Three-Dimensional Optothermal Manipulation of Light-Absorbing Particles in Phase-Change Gel Media

Pavana Siddhartha Kollipara[#],

Walker Department of Mechanical Engineering, The University of Texas at Austin, Austin, Texas 78712, United States

Zilong Wu[#],

Materials Science and Engineering Program and Texas Materials Institute, The University of Texas at Austin, Austin, Texas 78712, United States

Kan Yao,

Walker Department of Mechanical Engineering, The University of Texas at Austin, Austin, Texas 78712, United States; Materials Science and Engineering Program and Texas Materials Institute, The University of Texas at Austin, Austin, Texas 78712, United States

Dongdong Lin,

Qian Xuesen Collaborative Research Center of Astrochemistry and Space Life Sciences, Department of Microelectronic Science and Engineering, Ningbo University, Ningbo, Zhejiang 315211, China

Zhengyu Ju,

Materials Science and Engineering Program and Texas Materials Institute, The University of Texas at Austin, Austin, Texas 78712, United States

Xiaotian Zhang,

Department of Materials Science and Engineering, The Pennsylvania State University, University Park, Pennsylvania 16802, United States

Taizhi Jiang,

Corresponding Author: **Yuebing Zheng** – Walker Department of Mechanical Engineering, The University of Texas at Austin, Austin, Texas 78712, United States; Materials Science and Engineering Program and Texas Materials Institute, The University of Texas at Austin, Austin, Texas 78712, United States; zheng@austin.utexas.edu.

McKetta Department of Chemical Engineering and Texas Materials Institute, The University of Texas at Austin, Austin, Texas 78712, United States

Hongru Ding,
Walker Department of Mechanical Engineering, The University of Texas at Austin, Austin, Texas 78712, United States

Jie Fang,
Materials Science and Engineering Program and Texas Materials Institute, The University of Texas at Austin, Austin, Texas 78712, United States

Jingang Li,
Materials Science and Engineering Program and Texas Materials Institute, The University of Texas at Austin, Austin, Texas 78712, United States

Brian A. Korgel,
Materials Science and Engineering Program and Texas Materials Institute and McKetta Department of Chemical Engineering and Texas Materials Institute, The University of Texas at Austin, Austin, Texas 78712, United States

Joan M. Redwing,
Department of Materials Science and Engineering, The Pennsylvania State University, University Park, Pennsylvania 16802, United States; 2D Crystal Consortium, Materials Research Institute, The Pennsylvania State University, University Park, Pennsylvania 16802, United States

Guihua Yu,
Walker Department of Mechanical Engineering, The University of Texas at Austin, Austin, Texas 78712, United States; Materials Science and Engineering Program and Texas Materials Institute, The University of Texas at Austin, Austin, Texas 78712, United States

Yuebing Zheng
Walker Department of Mechanical Engineering, The University of Texas at Austin, Austin, Texas 78712, United States; Materials Science and Engineering Program and Texas Materials Institute, The University of Texas at Austin, Austin, Texas 78712, United States

Abstract

Rational manipulation and assembly of discrete colloidal particles into architected superstructures have enabled several applications in materials science and nanotechnology. Optical manipulation techniques, typically operated in fluid media, facilitate the precise arrangement of colloidal particles into superstructures by using focused laser beams. However, as the optical energy is turned off, the inherent Brownian motion of the particles in fluid media impedes the retention and reconfiguration of such superstructures. Overcoming this fundamental limitation, we present on-demand, three-dimensional (3D) optical manipulation of colloidal particles in a phase-change solid medium made of surfactant bilayers. Unlike liquid crystal media, the lack of fluid flow within the bilayer media enables the assembly and retention of colloids for diverse spatial configurations. By utilizing the optically controlled temperature-dependent interactions between the particles and their surrounding media, we experimentally exhibit the holonomic microscale control of diverse particles for repeatable, reconfigurable, and controlled colloidal arrangements in 3D. Finally, we demonstrate tunable light–matter interactions between the particles and 2D

materials by successfully manipulating and retaining these particles at fixed distances from the 2D material layers. Our experimental results demonstrate that the particles can be retained for over 120 days without any change in their relative positions or degradation in the bilayers. With the capability of arranging particles in 3D configurations with long-term stability, our platform pushes the frontiers of optical manipulation for distinct applications such as metamaterial fabrication, information storage, and security.

Graphical Abstract
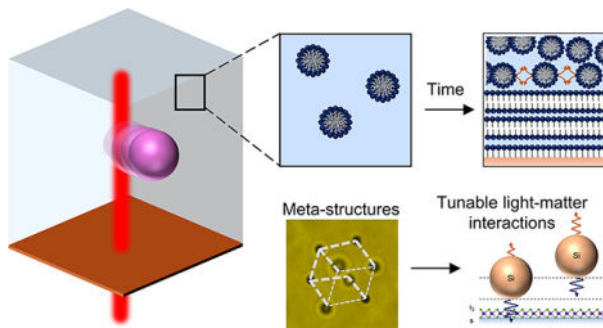
Keywords

optical tweezers; optothermal tweezers; bilayers; phase change; light–matter interactions; metamaterials; microfabrication

INTRODUCTION

Architected superstructures made of discrete colloidal particles have enabled many applications in photonics and optoelectronics.[1,2] For instance, the precise placement of these particles in rationally designed configurations has led to diverse resonant behaviors, generating strong optical fields in the subwavelength regime beyond the diffraction limit of light.[3–5] Several techniques such as self-assembly, electron-beam lithography, and 3D photolithography are proposed for the fabrication of superstructures using micro/nanoparticles as building blocks.[6–11] However, these techniques often result in static superstructures, which lack reconfigurability for their broader applications, such as rewritable information storage.

Optical manipulation has become a widely used methodology for manipulating various micro- and nanocolloids,[12,13] leading to numerous applications in physics and manufacturing.[14] By exploiting the optical gradient force, particles dispersed in either liquid media or a vacuum are trapped at the laser beam focus and manipulated in 3D[12,15,16] to fabricate desired superstructures. However, when the laser beam is switched off, the Brownian motion of particles hampers their position control, causing structural failure of the superstructures. Additional forces, such as van der Waals (vdW) forces,[17] chemical binding,[18] depletion,[19] thermoelectric force,[20] or gelation of hydrogels,[21] have been employed to immobilize the particles relative to each other, but are either restricted to 2D arrangements with limited reconfigurability or lack reconfigurable 3D structure fabrication.

Overcoming the Brownian motion, optical manipulation of colloids was also demonstrated on solid–air interfaces, either by exploiting surface tension gradients or formation of vapor bubbles due to optical heating, but are limited only to in-plane configurations.[22–26] Extending to 3D, researchers enabled the ejection of particles from one substrate to another for 3D nanoprinting applications and semiconductor particle manipulation by melting the glass fibers at high laser powers.[27,28] However, achieving reconfigurable and stable 3D colloidal arrangements by using optical manipulation is still elusive.

Here, we present a variant of optothermal manipulation utilizing phase change (OMPC) that simultaneously reduces the impact of Brownian motion and permits precise 3D colloidal arrangement of light-absorbing colloidal particles. The key component of our method is a phase-change solid medium composed of surfactant bilayers, which serves as a matrix to immobilize micro- and nanoparticles at room temperature. Although optical manipulation in liquid crystals has extensively been investigated and liquid crystals also display phase transitions, they are inherently in liquid phase, and the particles cannot be immobilized after switching off the laser beam.[29] Upon exposure to a laser beam, the particles absorb light and get heated, locally altering the phase of the solid medium, which allows for directional forces exerted on the particles in a controlled manner. When the laser is turned off, the matrix returns to its original phase and the particles remain immobilized in their new positions. With this reversible phase-change medium, 3D optical microstructures can be fabricated and reconfigured for diverse applications, including volumetric displays, information storage, and chiral superstructure fabrication.

RESULTS AND DISCUSSION

Working Mechanism of OMPC.

Colloidal particles are dispersed in an octyl trimethylammonium chloride surfactant solution, and the suspension is drop-coated onto a glass substrate and left open to the atmosphere (see Methods). The surfactant molecules in the bulk liquid are either adsorbed on the particle surface or form micelles in the bulk liquid. As the water in the suspension evaporates, the concentration of the micelles in the solution increases, eventually causing the micelles to rupture and reform into surfactant bilayers on the particle and glass surfaces (Figure S1).[30,31] Upon the complete evaporation of free water, the particles are embedded in the resultant surfactant matrix in its coagel phase (a tight, lamellar, and hydrated, surfactant bilayer phase) at ambient temperature (Figure 1a). The water between the bilayers is retained (not evaporated) due to nanoconfinement and adhesion forces between the hydrophilic headgroup of surfactant molecules and the water molecules (Figure 1b and Figure S1).[32] Thermogravimetric analysis and Fourier-transform infrared spectroscopy prove the quantitative existence of water within the bilayer after 2 weeks post-preparation (Figure S2). When a particle is irradiated with a laser beam, the absorption of light results in a local temperature increase around the particle. This increases the interlamellar space between the bilayers surrounding the particle, which is occupied by water that migrates from the cold section of the bilayers away from the particle.[33,34] As temperature increases beyond the transition temperature (T_{TR}), the enhanced atomistic vibrations result in phase transition from the coagel to gel phase (Figure 1b), which reduces the rigidity of the medium.[35]

Additionally, the fast laser heating and cooling induces breaks in the bilayer structure that further reduce the structure's integrity, enabling the particle motion.[32] Differential scanning calorimetry analysis is performed to determine the phase transition temperature of the matrix (Figure S2; see Methods). In its gel phase, the surfactant matrix exerts considerably lower resistance on the particles, which enables OMPC of the particles. The bilayers revert to their coagel state after switching off the laser beam, thereby immobilizing the particles in their new position.

The enhanced temperature of the particle, which is essential for achieving a phase transition, depends on its position (X_P, Z_P) relative to the focal point of the laser beam. Figure 1c highlights the simulated average surface temperature of a 1.5 μm silicon (Si) particle embedded in the coagel phase of octyl trimethylammonium chloride surfactant as a function of its position relative to a 660 nm laser beam at the optical power of 3.5 mW (see Methods). Although the temperatures are high, the laser–particle distance increases within a few milliseconds, thereby reducing the effective temperature of the particles and surrounding media. The subsecond manual repositioning of the laser beam provides sufficient time to repair the changes to the bilayer structure. The dashed white lines demarcate the gel phase (center) and coagel phase of the bilayer structure. We performed molecular dynamics (MD) simulations to evaluate the interaction energy per unit area (e_{vdW}) between the Si surface and surfactant bilayers as a function of temperature (Figure S3, see Methods). During this evaluation, we model the surface of the micrometer-sized Si particles as a flat plane. This approximation allows us to analyze the local interactions between the particle and the bilayer medium. It must be noted that the interaction energy per unit area is linearly proportional to the temperature. The total interaction energy (E_{vdW}) between the Si particle and the medium is then calculated by integrating e_{vdW} around the particle surface as $E_{vdW} = \int e_{vdW}(T)dA = e_{vdW}(T_{avg})A_p$, which varies as the particle's position with respect to the focus of the laser beam (Figure 1d). Here, T and T_{avg} are the local surface temperature on the particle and the average surface temperature of the particle, respectively, and A_p is the surface area of the particle. The total interaction energy strongly varies in the X direction compared to that in the Z direction owing to the narrow beam focus. Due to the undulations and local gaps in bilayers, the local temperature distribution around the particle is disregarded. The interaction energy estimation uses the average temperature of the particle.

For further investigation, the vdW force (F_{vdW}) between the particle and the surfactant bilayers is evaluated based on the interaction energy landscape as $F_{vdW} = -\nabla E_{vdW}$ (Figure 1e). The nano-newton-scale force is expected due to the highly localized viscous gel phase surrounding the particle and the high elastic modulus of coagel phase surrounding the gel phase.[36] Therefore, the particle can be manipulated only when surrounded by the medium in its gel phase (highlighted by the white lines in Figure 1c). However, an overestimation of force is possible because the bilayers are assumed to be uniformly distributed around the particle. Bilayers usually demonstrate undulations with wavelengths up to submicron scales during their formation, which cannot be incorporated in nanometerscale MD simulations.[31,37] These undulations vary the distance between the particle surface and the bilayers, resulting in a reduced interaction energy and lower-than-expected force magnitudes. Despite the precision of the forces, the average force directionality still holds

over a manipulation time scale spanning several seconds. It must be noted that the Si particles experience optical forces on the order of pN/mW (Figure S4). The optical forces are 3 orders lower in magnitude compared to the vdW forces and hence are ignored in our further analysis.

When the laser beam is shined directly on the particle center, the vdW force directs the particle along or against the laser beam axis (+Z or −Z directions), depending on the focal plane position with respect to the particle. This is because the radial force (in the X and Y directions) vanishes due to axial symmetry. However, when the laser is centered with a small offset from the particle center, the radial force dominates, resulting in the motion of the particle perpendicular to the laser beam axis. Consequently, three manipulation modes are possible as highlighted in Figure 1f: "push", representing the particle motion along the beam axis (+Z), when $X_P \sim 0$ and $Z_P > Z_{lim}$; "pull", representing the particle motion against the beam axis (−Z), when $X_P \sim 0$ and $Z_P < Z_{lim}$; and "nudge", representing the particle motion perpendicular to the beam axis (±X), when $|X_P| > 0.1$ μm. Here, Z_{lim} is the transition point between the "push" and "pull" modes of manipulation where its average surface temperature is the maximum. Particles close to the substrate experienced slightly elevated friction, which was overcome by increasing the laser power by ~10%. However, the force directionality and manipulation mechanism remained the same as those of particles located within the bulk medium.

Holonomic Control of Colloidal Particles Using OMPC.

Harnessing the ability of immobilization, we experimentally demonstrate diverse modes of 3D manipulation using Si microparticles. By positioning the laser beam focus at required spots, we demonstrate the pushing (Figure 2a), pulling (Figure 2b), and nudging (Figure 2c) modes of manipulation. In all three modes, the particle stayed in its final position after the laser was switched off. We further demonstrate the manipulation of particles in different sizes and materials, such as 500 nm Si particles, 150 nm gold nanoparticles, and 2.8 μm magnetic polystyrene (PS) particles containing 12% iron oxide (Figures S5–S7). To validate reversible phase-change, we also manipulate a single particle along the same path multiple times. As visualized in the dark-field microscopic images, there is no evident trace of particle motion, indicating that the surrounding medium is not damaged during the manipulation (Figure S8). Additionally, we did not observe any noticeable differences in the manipulation capabilities when the particle was manipulated in the same path. The 1.5 μm Si particles have been manipulated with an average speed of 3.7 μm/s, while the 150 nm Au NPs with an average speed of 1.5 μm/s. However, the local bilayer structure uncertainties, undulations, laser–particle distance uncertainty, and manual adjustment result in high uncertainty in the manipulation magnitude (~35%).

We further implemented OMPC on nanowires due to their importance in photonic circuits, sensing, and electronic devices.[38] Previously, optical tweezers were implemented in controlling the 3D orientation of nanowires but required continuous incidence of the laser beam or a substrate to align the nanowire in a stagnant orientation.[39] Here, by focusing the laser beam on one end of the nanowire, we achieve a localized phase change of the surfactant medium. This results in the controlled motion of the laser-focused end, while

the other end acts as an immobilized hinge, enabling the rotation of the nanowire in both in-plane (azimuthal) and out-of-plane (polar) directions (Figure 2d,e, Figure S9). Although we demonstrated only rotation of NWs, the translation of asymmetric nanowires with such high aspect ratio requires a defocused laser beam to induce phase-change around the entire wire, which suffers from a high power requirement and lack of directionality. To enable simultaneous translation and rotation of nanowires, we propose the use of multiple focused laser beams to simultaneously induce phase-change and enable the directional control of different locations on the nanowires. This requires an algorithmic approach involving a feedback loop between the laser beam controller and the camera, which is outside the scope of this article.

Versatile Microstructure Fabrication Using OMPC.

In liquid media, microstructures fabricated using optical tweezers require the simultaneous manipulation of multiple particles, which necessitates the continuous deployment of independent laser beams from advanced light-modulation devices. Here, we exploit the gel–coagel phase transition and subsequent particle immobilization using OMPC over conventional optical manipulation for superstructure fabrication. First, we exhibit the sequential formation of a cube (of edge length 10 μm) using a single laser beam. Figure 3a shows a schematic of the cube and sequential microscopic images of its formation. To ensure visibility of all of the vertices, the cube is assembled in a rotated configuration (Figure S10). Furthermore, to demonstrate the reconfigurability of OMPC, seven particles are initially manipulated to generate a 2D pattern representing the shape of digit "2" (Figure 3b (i)). The particles are then manipulated in 3D to form the digit "3" (Figure 3b (ii)) lying on a virtual plane tilted with respect to the substrate and laser beam axis. The two optical images show the tilted planar configuration by focusing on the two extreme particles in the arrangement, as indicated by the gradual defocus (blurring) among the particles. The intentional translation of particles to reconfigure "2" to "3" showcases both 2D and 3D maneuverability of the technique.

Finally, we demonstrate the manipulation of particles on high-curvature surfaces to explore the adaptability of our technique in arbitrary domains required for complex metastructure formation. We manipulated a 1.5 μm Si particle on a 10 μm non-absorbing PS particle representing a high-curvature surface (schematic in Figure 3c). The microscopic images in Figure 3c show sequential top-view images of the Si particle moving across the PS particle surface. Due to its proximity to the PS particle, the absorption of the laser beam by the Si particle and its corresponding temperature increment and the directional forces are expected to be different from Figure 1c–e. Despite this, the particle can still be effectively manipulated, demonstrating the versatility of the manipulation technique. Nevertheless, the effectiveness of the technique diminishes in the presence of high-concentration colloidal systems. This is attributed to the distortion of the laser beam focus caused by interactions between light and particles. Potential solutions to address this drawback involve utilizing a spatial light modulator to modify both the amplitude and phase of the incoming laser beam.[40]

Tunable Light–Matter Interactions Using OMPC.

With the simultaneous manipulation and positioning of particles using OMPC, we further demonstrate tunable light–matter interactions between the particles and 2D materials introduced on the substrate. Recent years have witnessed a growth in research of 2D materials such as graphene and transition metal dichalcogenides (TMDCs), particularly in the field of photonic devices.[41,42] Controlling the excitonic emission properties of 2D materials has useful applications in photodetection, lasers, and optical sensing.[43–45] Recently, Si nanowires and nanoparticles served as optical antennas to modify the emission properties of monolayer TMDCs.[46,47] However, they are limited to a fixed ultrasmall emitter–particle distance using an optically inactive spacer layer, which needs to be fabricated through drop-casting or physical vapor deposition methods. The non-tunability of the spacer thickness makes it challenging to obtain tunable light–matter interactions, hampering the optimal performance of the photonic devices. Herein, as a case study, we use monolayer WSe_2 and Si particles as antennas to understand the tunability of the 2D materials' excitonic emission by altering the Si particles' distance from the monolayer (Figure 4a). Figure 4b presents the forward-to-backward (F/B) emission ratio as functions of emitter–sphere distance and wavelength, where the 2D material is modeled as a horizontal electric dipole emitter for simplification, facilitating the analysis based on generalized Mie theory.[46,48]

Here, we define the forward emission direction toward the Si particle and backward emission direction being the opposite toward the substrate. Given that a plain WSe_2 monolayer has its exciton emission at ~750 nm (see Figure S11 for the photoluminescence (PL) spectrum), we further focus our attention on the small spectral interval around this wavelength. Figure 4c compares the normalized PL spectra when the Si particle was positioned 500 nm (Z_1) and 1000 nm (Z_2) above the WSe_2 layer. A noticeable shift is seen between the two spectra, and both differ from the Lorentzian line shape of the PL signal of bare WSe_2 (Figure 4c) by exhibiting additional peaks at longer wavelengths. These observations can be explained well by the generalized Mie theory. When a particle is placed near an emitter at a certain distance, the radiative enhancement is a function of wavelength, as can be deduced from the fringes in Figure 4b. Therefore, the PL intensity of a coupled system is the product of the PL of bare WSe_2 and the radiative enhancement factor, and the latter gives rise to wavelength-dependent variations on top of the original Lorentzian line shape. On the other hand, because Mie resonances of the particle are excited by an emitter at different distances differently, the wavelengths of the maxima and minima of the radiative enhancement vary as the emitter–particle distance is changed, resulting in a shift to the peak of the PL spectrum. Although only backward emission can be measured in our experimental setup (Figure S12), we simulated the radiation pattern at the two distinct heights of Z_1 and Z_2, as shown in Figure 4d. The emitter–particle distance dramatically affects the relative weights of the excited Mie resonances, which determine the angular distributions of the emitted photons. It must be noted that the PL signal in Figure 4c is a combination of the bare WSe_2 spectrum (Figure S11) and the periodic peaks in Figure 4b that correspond to the dipole–particle distance and wavelength. The additional shoulder in Figure 4c is a natural manifestation of the spherical harmonics of dipole–particle interactions from the Mie theory. For this analysis, we only consider the shift of the peak of the bare WSe_2 spectrum.

CONCLUSIONS

This work has successfully demonstrated the 3D optical manipulation of colloidal particles within a phase-change solid medium created by the formation of surfactant bilayers. By exploiting the optical heating of the particles and the nanoscale water confinement within the surfactant bilayers, we locally induce the reversible phase transition between the coagel and gel states of the medium and enable the site-selective and on-demand manipulation and immobilization of the particles. Our simulation results indicate that the temperature-dependent interaction energy between the particle and bilayer surroundings during phase change is responsible for the light-directed particle motion across different sizes and materials. Leveraging this advantage, we generated several 3D superstructures in a reversible and reconfigurable fashion. Upon switching off the laser beam, the surfactant matrix is reversed into a coagel state, where the particles are immobilized for extended periods (up to four months, as shown in Figure S13). Applications of OMPC other than manufacturing, such as tunable light–matter interactions at the microscale, were also demonstrated successfully.

Compared to other techniques such as acoustic tweezers and dielectrophoretic manipulation, which are also liquid-based and employ continuous energy fields (ultrasonic or electric) to manipulate particles,[49–52] our technique clearly offers several advantages like lower energy requirement, 3D manipulation, and high stability. However, we recognize that additional efforts are necessary to overcome some of the current limitations of OMPC, such as the lack of precise evaluation of the Z coordinate from images and low manipulation throughput. In our case study with trimethyloctylammonium chloride (TOMAC), we have demonstrated a good performance of this manipulation technique by optimizing the bilayer preparation protocol. However, an in-depth understanding is required to exploit other surfactants, polymeric molecules, and phospholipids, which exhibit multiple phases at distinct transition temperatures.[53,54] Depending on the laser-induced temperature increase and local phase change, we achieve particle trapping followed by immobilization, which features advantages of both optical tweezers and OMPC. Additionally, OMPC has an accuracy of 70 and 170 nm for micron-sized particles for in-plane and out-of-plane manipulation, respectively (Figure S14). This resolution is limited by particle-toparticle variations in their thermal conductivity and heat generation, multifaceted nature of particles, and pixelated imaging capabilities required for calibration. Although we demonstrated the manipulation of 150 nm Au particles, manipulation of sub-500 nm particles becomes challenging due to the micron-scale undulation of the bilayers and precise positioning of the laser beam with respect to the particle center. Future work could include evaluating new surfactants, optimizing the bilayer preparation protocols for minimal undulations, and improving the precision of laser and particle positioning through image-based feedback algorithms to automate the manipulation process and reduce human error.[55] Specifically, by optimizing the evaporation temperature and humidity during the bilayer formation of surfactants or phospholipids, we can achieve better control on the water content and undulations of the bilayers, enabling the manipulation of smaller particles while retaining the immobilization characteristic of OMPC. Merging optimized bilayers with intelligent feedback control loops, we can simultaneously enhance the accuracy and speed of the manipulation process. With the

proposed technique and future advances, we believe that OMPC has the potential to enable various photonic and nanotechnology applications.

METHODS

Synthesis of Si Particles (1.5 and 0.5 *μ*m).

The synthesis was performed using a 10 mL titanium batch reactor from the High-Pressure Equipment Company (HiP Co.). Inside a nitrogen-filled glovebox, 126 *μ*L of trisilane (Si_3H_8, 100%, Voltaix) and 5.5 mL of anhydrous *n*-hexane (anhydrous, 95%, Sigma-Aldrich) were loaded in the reactor. The amount of trisilane affects the particle size, and the combination of the *n*-hexane amount and reaction temperature determines the necessary pressure inside the reactor during heating. For example, for the 1.5 *μ*m Si particles, a temperature of 470 °C, an *n*-hexane amount of 5.5 mL, and a reaction pressure of 34.5 MPa were used. The synthesized Si particles have a hydrogen concentration of 5%.[56,57] After the reagents were added, the reactor was then sealed in the glovebox and tightened with a wrench and vise. Heated for 10 min in a heating block to allow the complete decomposition of trisilane, the reactor was then cooled to room temperature with an ice bath. The resulting colloidal Si particles were extracted and washed three times with chloroform (99.9%, Sigma-Aldrich) using a centrifuge at 8000 rpm for 5 min.

Surfactant Bilayer Preparation.

Glass coverslips are cleaned and sonicated in isopropyl alcohol followed by DI water for 10 min each. The sample is then blow-dried using a N_2 stream. TOMAC (Possible Missions Inc.) is dissolved in DI water to make a 1 M solution. Care is taken to avoid frothing during the preparation. The TOMAC solution is diluted to 0.5 M by addition of DI water. Si particles (1.5 *μ*m) dispersed in ethanol are diluted to 10% in DI water (10% ethanol and 90% DI water) followed by centrifugation at 4500 rpm for 10 min, pipetted out of the solvent, and redispersed through sonication in DI water for 1 min. The dilution, centrifugation, and sonication are repeated twice to obtain the Si particles dispersed in DI water. Finally, the particle suspension in water is diluted 100-fold by a 0.5 M TOMAC solution, followed by ultrasonication for 1 min to obtain uniformly dispersed Si particles in 0.5 M TOMAC solution. The final suspension is then drop-coated on clean glass coverslips at a temperature of 40 °C in open air (room temperature 23.6 °C and 18% RH) and baked for 3.5 h for complete evaporation of free water. As water evaporates, the TOMAC concentration increases and bilayers are formed. Note that higher volumes for drop coating would require a longer baking time. The baking temperature (40 °C) is a major factor as the evaporation rate dictates the formation dynamics of the bilayer. For other surfactants, the baking temperature needs to be optimized.[54] Postbaking, the thickness of the bilayer is estimated to vary between 20 and 50 *μ*m at different locations as shown in Figure S15.

Thermogravimetric Analysis and Differential Scanning Calorimetry Analysis of Surfactant Bilayers.

The TG analysis was conducted using a thermogravimetric analyzer (PerkinElmer, TGA 4000) with a N_2 flow rate of 20 mL/min and a heating rate of 5 °C/min. The phase transition behaviors were evaluated with a differential scanning calorimeter (TA Instruments, DSC

250). The sample was presealed in an airtight aluminum container, and the scan rate for the DSC test was set as 5 °C/min.

Evaluation of Temperature Increase of Si Particles under Laser Excitation.

The wave optics module and heat transfer module in COMSOL v5.2a were used to simulate the laser heating of 1.5 μm Si particles. The Si particles and the surrounding medium were modeled as a sphere in a cube of $20 \times 20 \times 20$ μm^3, representing the surfactant medium. For the wave optics module, scattering boundary conditions were used on the exterior surfaces of the simulation domain, and a Gaussian beam set with a known power (measured from experiments) was incorporated as a background field. For the heat transfer module, the boundary of the surfactant medium was set at a constant 300 K. Using multiphysics coupling, the heat generated by the Si particle was evaluated by using joule (electric) heating. A fine mesh of 50 nm was used for Si particles, and a maximum mesh size of 150 nm was utilized for the surfactant medium. The dielectric function of silicon was obtained from Aspens and Studna.[58] The refractive index of the surfactant was taken as 1.44 with no loss, leaving the only heat source in the system being the Si particle, as observed in our experiments. The thermal conductivity, density, and heat capacity of the surfactant were taken as $-0.87 + 8.9 \times 10^{-3} T - 1.583 \times 10^{-5} T^2 + 7.975 \times 10^{-9} T^3$ W·m^{-1}·K^{-1}, 838.46 $+ 1.4T - 0.003 T^2$ kg/m^3, and $12\,010 - 80.4 T + 0.31 T^2 - 5.38 \times 10^{-4} T^3$ J·kg^{-1}· K^{-1}, respectively, where T represents the temperature (in K). The thermal conductivity, density, and heat capacity of silicon were taken as 22 W·m^{-1}·K^{-1}, 2329 kg/m^3, and 700 J·kg^{-1}·K^{-1} respectively. The laser parameters were set as 660 nm for the wavelength, 500 nm for the beam waist, and 3.5 mW for power.

MD Simulations to Evaluate the Interaction Potential between the Si Particle and the Surfactant Bilayers.

All simulations were performed by using version 2019 of the GROMACS MD simulation package. The dimensions of the simulation box were $7.5 \times 7.5 \times 10$ nm with 400 TOMAC surfactant monomers. We employed the all-atom optimized potentials for liquid simulations (OPLS-AA) force field in all our simulations.[59] Equations of motions were integrated with the leapfrog algorithm,[60] and the time step was 2 fs. The charge and vdW parameters of TOMAC surfactant monomers were taken from refs 61 and 62 with the Si substrate fixed. The cutoff for the nonbonded interaction and the electrostatic interaction was set to 12 Å. The electrostatic interaction was calculated by applying the SPME method, and the trajectory was saved every 100 steps. Periodic boundary conditions were applied in all directions. The MD simulations were then performed at discrete temperatures ranging from 310 to 700 K to obtain the temperature-dependent interaction energies between the particle and the surrounding surfactant.

Evaluation of F/B Ratio (Simulation).

The map of F/B emission ratio and radiation patterns in Figure 4 were computed using generalized Mie theory.[48] For the present system, a tangential electric dipole, a Si microsphere, a host medium with refractive index $n = 1.4$, and a dipole–sphere distance in the range 1–1200 nm were used in the analysis. Once the electromagnetic fields outside the particle were solved, radiation patterns could be directly obtained by evaluating the

radial component of the Poynting vector on a spherical surface in the far field. The results were verified by FDTD simulations. Likewise, the F/B emission ratio was calculated based on integrating the radial component of the Poynting vector over spherical caps in the forward (θ: 130–180°, φ: 0–360°) and backward (θ: 0–50°, φ: 0–360°) directions, which correspond to the NA of the objective. The integrations were computed as summations, with resolutions of 2° and 15° in the polar and azimuthal directions, respectively.

Synthesis and Transfer of WSe$_2$ Films.

Growth of Monolayer WSe$_2$.—Monolayer WSe$_2$ films were synthesized through a multistep gas-source metal–organic chemical vapor deposition (MOCVD) process. The system employed a vertical cold-wall reactor and used tungsten hexacarbonyl (W(CO)$_6$) and hydrogen selenide (H$_2$Se) as precursors. A 1×1 cm^2 double-sided polished c-plane sapphire was thoroughly rinsed with acetone, 2-propanol, nanostrip, and deionized water and dried with N$_2$ gas before using it as a substrate. Ultrahigh pure hydrogen gas was used as the carrier gas to maintain a total flow rate of 500 sccm and a reactor pressure of 700 Torr. When the growth started, a high W(CO)$_6$ flow rate of 1.8×10^{-3} sccm out of the bubbler was introduced into the reactor for 2 min, which was then reduced to 1.9×10^{-4} sccm for 60 min. The H$_2$Se flow rate was held constantly at 7 sccm, and the substrate temperature was maintained at 800 °C during the whole growth period.

Transfer of WSe$_2$ Films.—The MOCVD-grown monolayer WSe$_2$ was transferred onto the glass by using a wet transfer process. Poly(methyl methacrylate) (PMMA) was first spin-coated on the WSe$_2$ sample and maintained at room temperature overnight. The assembly was then immersed in hot water (~80 °C) for 5–10 min for WSe$_2$/sapphire delamination. The detached PMMA/WSe$_2$ film was picked up from the water onto the glass substrate and placed on a hot plate (~70 °C) for 10 min. Lastly, PMMA was removed with acetone, followed by rinsing with 2-propanol.

Optical Setup.: As for the 3D manipulation, a 660 nm laser beam (Laser Quantum, Opus 660) is passed through a 5× beam expander and directed into the objective (Nikon Plan Fluor 100× oil, NA 0.5–1.3) of an optical microscope (Nikon Ti-E) using several reflective mirrors. The surfactant matrix (as prepared in previous sections) is loaded onto the stage. A charged coupled device (CCD, Nikon DS-Fi3) is used to visualize particle manipulation.

As for the PL measurement, a 100× objective (Nikon T Plan SLWD 100×, NA 0.6) is used to collect the signal, and a spectrograph (Andor Shamrock 303i-B) with an EMCCD (Andor Newton DU970P) is used to measure the PL spectra of the 2D materials used in this work. Please refer to Figure S12 for the schematic of the experimental setup.

Supplementary Material

Refer to Web version on PubMed Central for supplementary material.

ACKNOWLEDGMENTS

REFERENCES

(1). Zhang B; Meng F; Feng J; Wang J; Wu Y; Jiang L Manipulation of Colloidal Particles in Three Dimensions via Microfluid Engineering. Adv. Mater 2018, 30 (22), 1707291.

(2). Caleap M; Drinkwater BW Acoustically trapped colloidal crystals that are reconfigurable in real time. Proc. Natl. Acad. Sci. U. S. A 2014, 111 (17), 6226–6230. [PubMed: 24706925]

(3). Luk'Yanchuk B; Zheludev NI; Maier SA; Halas NJ; Nordlander P; Giessen H; Chong CT The Fano resonance in plasmonic nanostructures and metamaterials. Nat. Mater 2010, 9 (9), 707–715. [PubMed: 20733610]

(4). Fan JA; Wu C; Bao K; Bao J; Bardhan R; Halas NJ; Manoharan VN; Nordlander P; Shvets G; Capasso F Self-Assembled Plasmonic Nanoparticle Clusters. Science 2010, 328 (5982), 1135–1138. [PubMed: 20508125]

(5). Hakala TK; Rekola HT; Väkeväinen AI; Martikainen JP; Necada M; Moilanen AJ; Törmä P Lasing in dark and bright modes of a finite-sized plasmonic lattice. Nat. Commun 2017, 8 (1), 13687. [PubMed: 28045047]

(6). Zhu C; Meng G; Zheng P; Huang Q; Li Z; Hu X; Wang X; Huang Z; Li F; Wu N A Hierarchically Ordered Array of Silver-Nanorod Bundles for Surface-Enhanced Raman Scattering Detection of Phenolic Pollutants. Adv. Mater 2016, 28 (24), 4871–4876. [PubMed: 27112639]

(7). Yang K; Yao X; Liu B; Ren B Metallic Plasmonic Array Structures: Principles, Fabrications, Properties, and Applications. Adv. Mater 2021, 33 (50), 2007988.

(8). Staude I; Miroshnichenko AE; Decker M; Fofang NT; Liu S; Gonzales E; Dominguez J; Luk TS; Neshev DN; Brener I; et al. Tailoring Directional Scattering through Magnetic and Electric Resonances in Subwavelength Silicon Nanodisks. ACS Nano 2013, 7 (9), 7824–7832. [PubMed: 23952969]

(9). Chong KE; Hopkins B; Staude I; Miroshnichenko AE; Dominguez J; Decker M; Neshev DN; Brener I; Kivshar YS Observation of Fano Resonances in All-Dielectric Nanoparticle Oligomers. Small 2014, 10 (10), 1985–1990. [PubMed: 24616191]

(10). Wang K; Park SH; Zhu J; Kim JK; Zhang L; Yi GR Self-Assembled Colloidal Nanopatterns toward Unnatural Optical Meta-Materials. Adv. Funct. Mater 2021, 31 (12), 2008246.

(11). Jin F; Liu J; Zhao Y-Y; Dong X-Z; Zheng M-L; Duan X-M λ/30 inorganic features achieved by multi-photon 3D lithography. Nat. Commun 2022, No. 1357.

(12). Maragó OM; Jones PH; Gucciardi PG; Volpe G; Ferrari AC Optical trapping and manipulation of nanostructures. Nat. Nanotechnol 2013, 8 (11), 807–819. [PubMed: 24202536]

(13). Gao D; Ding W; Nieto-Vesperinas M; Ding X; Rahman M; Zhang T; Lim C; Qiu C-W Optical manipulation from the microscale to the nanoscale: fundamentals, advances and prospects. Light: Science & Applications 2017, 6, No. e17039.

(14). Melzer JE; McLeod E Assembly of multicomponent structures from hundreds of micron-scale building blocks using optical tweezers. Microsystems & Nanoengineering 2021, 7, No. 45.

(15). Magrini L; Rosenzweig P; Bach C; Deutschmann-Olek A; Hofer SG; Hong S; Kiesel N; Kugi A; Aspelmeyer M Real-time optimal quantum control of mechanical motion at room temperature. Nature 2021, 595 (7867), 373–377. [PubMed: 34262213]

(16). Deli U; Reisenbauer M; Dare K; Grass D; Vuleti V; Kiesel N; Aspelmeyer, M. Cooling of a levitated nanoparticle to the motional quantum ground state. Science 2020, 367 (6480), 892–895. [PubMed: 32001522]

(17). Urban AS; Lutich AA; Stefani FD; Feldmann J Laser Printing Single Gold Nanoparticles. Nano Lett. 2010, 10 (12), 4794–4798. [PubMed: 20957994]

(18). Walker D; Singh DP; Fischer P Capture of 2D Microparticle Arrays via a UV-Triggered Thiol-yne "Click" Reaction. Adv. Mater 2016, 28 (44), 9846–9850. [PubMed: 27717081]

(19). Lin L; Zhang J; Peng X; Wu Z; Coughlan ACH; Mao Z; Bevan MA; Zheng Y Opto-thermophoretic assembly of colloidal matter. Science Advances 2017, 3 (9), No. e1700458.

(20). Lin L; Lepeshov S; Krasnok A; Jiang T; Peng X; Korgel BA; Alú A; Zheng Y All-optical reconfigurable chiral meta-molecules. Mater. Today 2019, 25, 10–20.

(21). Peng X; Li J; Lin L; Liu Y; Zheng Y Opto-Thermophoretic Manipulation and Construction of Colloidal Superstructures in Photocurable Hydrogels. ACS Applied Nano Materials 2018, 1 (8), 3998–4004. [PubMed: 31106296]

(22). Li J; Kollipara PS; Liu Y; Yao K; Liu Y; Zheng Y Opto-Thermocapillary Nanomotors on Solid Substrates. ACS Nano 2022, 16 (6), 8820–8826. [PubMed: 35594375]

(23). Li J; Liu Y; Lin L; Wang M; Jiang T; Guo J; Ding H; Kollipara PS; Inoue Y; Fan D Optical nanomanipulation on solid substrates via optothermally-gated photon nudging. Nat. Commun 2019, 10, No. 5672.

(24). Li J; Wang M; Wu Z; Li H; Hu G; Jiang T; Guo J; Liu Y; Yao K; Chen Z; et al. Tunable Chiral Optics in All-Solid-Phase Reconfigurable Dielectric Nanostructures. Nano Lett. 2021, 21 (2), 973–979. [PubMed: 33372805]

(25). Meng F; Hao W; Yu S; Feng R; Liu Y; Yu F; Tao P; Shang W; Wu J; Song C; et al. Vapor-Enabled Propulsion for Plasmonic Photothermal Motor at the Liquid/Air Interface. J. Am. Chem. Soc 2017, 139 (36), 12362–12365. [PubMed: 28837327]

(26). Dietrich K; Jaensson N; Buttinoni I; Volpe G; Isa L Microscale Marangoni Surfers. Phys. Rev. Lett 2020, 125, No. 098001.

(27). Alam MS; Zhan Q; Zhao C Additive Opto-Thermomechanical Nanoprinting and Nanorepairing under Ambient Conditions. Nano Lett. 2020, 20 (7), 5057–5064. [PubMed: 32502352]

(28). Zhang J; Wang Z; Wang Z; Zhang T; Wei L In-fibre particle manipulation and device assembly via laser induced thermocapillary convection. Nat. Commun 2019, 10, No. 5206.

(29). Trivedi R; Engström D; Smalyukh I Optical manipulation of colloids and defect structures in anisotropic liquid crystal fluids. Journal of Optics 2011, 13 (4), 044001.

(30). Anderson TH; Min Y; Weirich KL; Zeng H; Fygenson D; Israelachvili JN Formation of Supported Bilayers on Silica Substrates. Langmuir 2009, 25 (12), 6997–7005. [PubMed: 19354208]

(31). Abraham S; Heckenthaler T; Bandyopadhyay D; Morgenstern Y; Kaufman Y Quantitative Description of the Vesicle Fusion Mechanism on Solid Surfaces and the Role of Cholesterol. J. Phys. Chem. C 2018, 122 (40), 22985–22995.

(32). Abraham S; Heckenthaler T; Morgenstern Y; Kaufman Y Effect of Temperature on the Structure, Electrical Resistivity, and Charge Capacitance of Supported Lipid Bilayers. Langmuir 2019, 35 (26), 8709–8715. [PubMed: 31244251]

(33). Yamamoto T; Yagi Y; Hatakeyama T; Wakabayashi T; Kamiyama T; Suzuki H Metastable and stable phase diagrams and thermodynamic properties of the cetyltrimethylammonium bromide (CTAB)/water binary system. Colloids Surf., A 2021, 625, 126859.

(34). Chapman D Phase transitions and fluidity characteristics of lipids and cell membranes. Q. Rev. Biophys 1975, 8 (2), 185–235. [PubMed: 1103214]

(35). Et-Thakafy O; Guyomarc'h F; Lopez C Young modulus of supported lipid membranes containing milk sphingomyelin in the gel, fluid or liquid-ordered phase, determined using AFM force spectroscopy. Biochimica et Biophysica Acta (BBA) - Biomembranes 2019, 1861 (9), 1523–1532. [PubMed: 31295476]

(36). Israelachvili JN 20 - Soft and Biological Structures. In Intermolecular and Surface Forces (Third ed.); Israelachvili JN, Ed.; Academic Press, 2011; pp 535–576.

(37). Heine D; Rammohan A; Balakrishnan J Atomistic simulations of the interaction between lipid bilayers and substrates. Mol. Simul 2007, 33 (4–5), 391–397.

(38). Yan Z; Jureller JE; Sweet J; Guffey MJ; Pelton M; Scherer NF Three-Dimensional Optical Trapping and Manipulation of Single Silver Nanowires. Nano Lett. 2012, 12 (10), 5155–5161. [PubMed: 22931238]

(39). Pauzauskie PJ; Radenovic A; Trepagnier E; Shroff H; Yang P; Liphardt J Optical trapping and integration of semiconductor nanowire assemblies in water. Nat. Mater 2006, 5 (2), 97–101. [PubMed: 16429143]

(40). Tang X; Xu Y; Shen Y; Rong W Accurately measuring phase profiles of structured light in holographic optical tweezers. Optics & Laser Technology 2023, 160, 109068.

(41). Xia F; Wang H; Xiao D; Dubey M; Ramasubramaniam A Two-dimensional material nanophotonics. Nat. Photonics 2014, 8 (12), 899–907.

(42). Turunen M; Brotons-Gisbert M; Dai Y; Wang Y; Scerri E; Bonato C; Jöns KD; Sun Z; Gerardot BD Quantum photonics with layered 2D materials. Nature Reviews Physics 2022, 4 (4), 219–236.

(43). Mak KF; Shan J Opportunities and challenges of interlayer exciton control and manipulation. Nat. Nanotechnol 2018, 13 (11), 974–976. [PubMed: 30397289]

(44). Mak KF; Shan J Photonics and optoelectronics of 2D semiconductor transition metal dichalcogenides. Nat. Photonics 2016, 10 (4), 216–226.

(45). Du W; Li C; Sun J; Xu H; Yu P; Ren A; Wu J; Wang Z Nanolasers Based on 2D Materials. Laser & Photonics Reviews 2020, 14 (12), 2000271.

(46). Cihan AF; Curto AG; Raza S; Kik PG; Brongersma ML Silicon Mie resonators for highly directional light emission from monolayer MoS2. Nat. Photonics 2018, 12 (5), 284–290.

(47). Fang J; Wang M; Yao K; Zhang T; Krasnok A; Jiang T; Choi J; Kahn E; Korgel BA; Terrones M; et al. Directional Modulation of Exciton Emission Using Single Dielectric Nanospheres. Adv. Mater 2021, 33 (20), 2007236.

(48). Yao K; Zheng Y Directional light emission by electric and magnetic dipoles near a nanosphere: an analytical approach based on the generalized Mie theory. Opt. Lett 2021, 46 (2), 302–305. [PubMed: 33449012]

(49). Ding X; Lin S-CS; Kiraly B; Yue H; Li S; Chiang IK; Shi J; Benkovic SJ; Huang TJ On-chip manipulation of single microparticles, cells, and organisms using surface acoustic waves. Proc. Natl. Acad. Sci. U. S. A 2012, 109 (28), 11105–11109. [PubMed: 22733731]

(50). Ahmed D; Lu M; Nourhani A; Lammert PE; Stratton Z; Muddana HS; Crespi VH; Huang TJ Selectively manipulable acoustic-powered microswimmers. Sci. Rep 2015, 5 (1), 9744. [PubMed: 25993314]

(51). Ahmed D; Ozcelik A; Bojanala N; Nama N; Upadhyay A; Chen Y; Hanna-Rose W; Huang TJ Rotational manipulation of single cells and organisms using acoustic waves. Nat. Commun 2016, 7 (1), 11085. [PubMed: 27004764]

(52). Barik A; Zhang Y; Grassi R; Nadappuram BP; Edel JB; Low T; Koester SJ; Oh S-H Graphene-edge dielectrophoretic tweezers for trapping of biomolecules. Nat. Commun 2017, 8 (1), No. 1867.

(53). Nagle JF Theory of the Main Lipid Bilayer Phase Transition. Annu. Rev. Phys. Chem 1980, 31 (1), 157–196.

(54). Colafemmina G; Palazzo G; Mateos H; Amin S; Fameau A-L; Olsson U; Gentile L The cooling process effect on the bilayer phase state of the CTAC/cetearyl alcohol/water surfactant gel. Colloids Surf., A 2020, 597, 124821.

(55). Yao K; Zheng Y Nanophotonics and Machine Learning; Springer Cham, 2023; DOI: 10.1007/978-3-031-20473-9.

(56). Harris JT; Hueso JL; Korgel BA Hydrogenated Amorphous Silicon (a-Si:H) Colloids. Chem. Mater 2010, 22 (23), 6378–6383.

(57). Jiang T; Khabaz F; Marne A; Wu C; Gearba R; Bodepudi R; Bonnecaze RT; Liechti KM; Korgel BA Mechanical properties of hydrogenated amorphous silicon (a-Si:H) particles. J. Appl. Phys 2019, 126 (20), 204303.

(58). Aspnes DE; Studna AA Dielectric functions and optical parameters of Si, Ge, GaP, GaAs, GaSb, InP, InAs, and InSb from 1.5 to 6.0 eV. Phys. Rev. B 1983, 27 (2), 985–1009.

(59). Kaminski GA; Friesner RA; Tirado-Rives J; Jorgensen WL Evaluation and Reparametrization of the OPLS-AA Force Field for Proteins via Comparison with Accurate Quantum Chemical Calculations on Peptides. J. Phys. Chem. B 2001, 105 (28), 6474–6487.

(60). Hockney RW; Goel SP; Eastwood JW Quiet highresolution computer models of a plasma. J. Comput. Phys 1974, 14 (2), 148–158.

(61). Pal S; Bagchi B; Balasubramanian S Hydration Layer of a Cationic Micelle, C10TAB: Structure, Rigidity, Slow Reorientation, Hydrogen Bond Lifetime, and Solvation Dynamics. J. Phys. Chem. B 2005, 109 (26), 12879–12890. [PubMed: 16852599]

(62). Ding H; Kollipara PS; Lin L; Zheng Y Atomistic modeling and rational design of optothermal tweezers for targeted applications. Nano Research 2021, 14 (1), 295–303. [PubMed: 35475031]
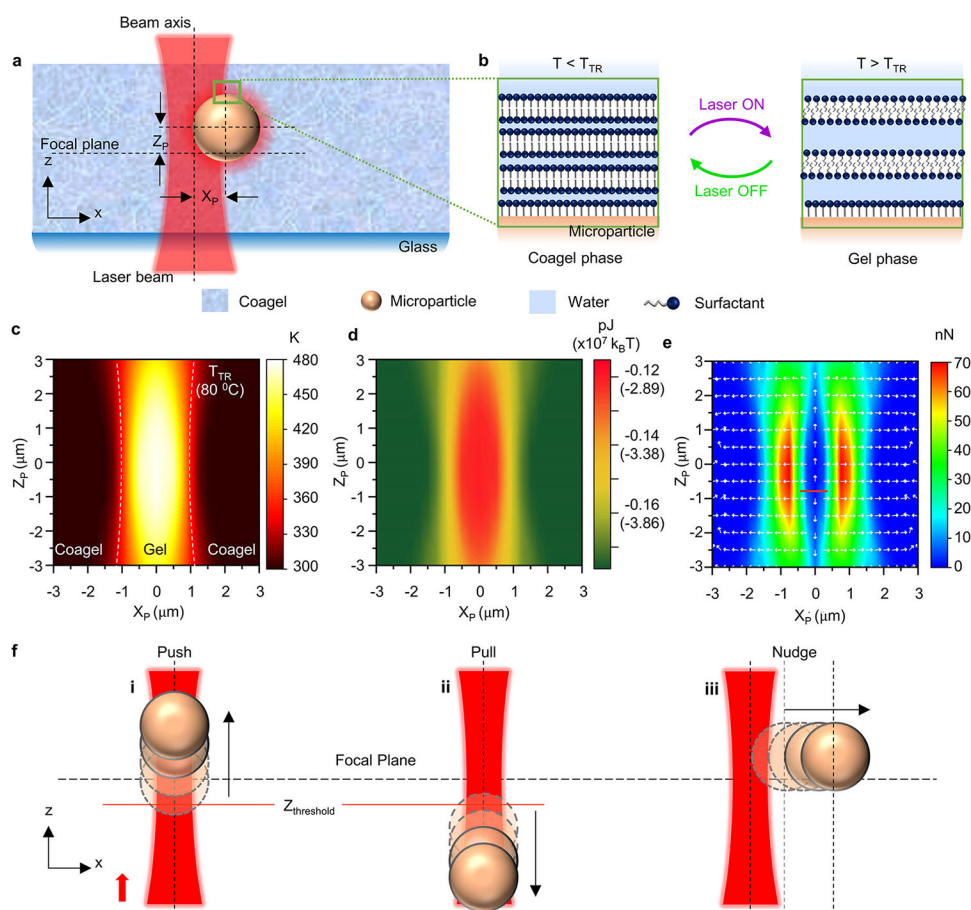
Figure 1.

Working mechanism of OMPC: (a) A laser beam is imposed on a particle embedded in the surfactant matrix. X_P and Z_P are the distances between the particle center and the laser beam center (intersection of beam axis and focal plane) along the X and Z directions, respectively. (b) Initially, the surfactant matrix around the particle exists in its coagel phase. When the laser is imposed on the particle, the temperature rises, and the increase in both the energy of the bilayers and the water content between the bilayers alters the interaction potential between the particle and the surfactant. As the temperature increases beyond a transition temperature (T_{TR}), the matrix reversibly changes its phase into a gel state, allowing the particle to be manipulated. (c) The average surface temperature of the particle with respect to its position from the laser beam center. The white dashed lines indicate the demarcation where the particle is surrounded by the surfactant in gel and coagel phases, at a transition temperature of 80 °C. (d) vdW interaction energy of the particle and surrounding bilayers as a function of the particle's position. (e) The magnitude and direction of the force acting on the particle. The red line at $(0, -0.75 \mu\text{m})$ indicates the $Z_{threshold}$, where the force is inverted when the laser beam is imposed directly on the particle. (f) The particle is pushed (i) or pulled (ii) when the particle center is above or below $Z_{threshold}$, respectively, when the laser beam is shined directly on the particle ($X_P \sim 0$). The particle is nudged (iii) perpendicular to the laser beam axis when the laser is shined with a lateral offset to the particle center (X_P
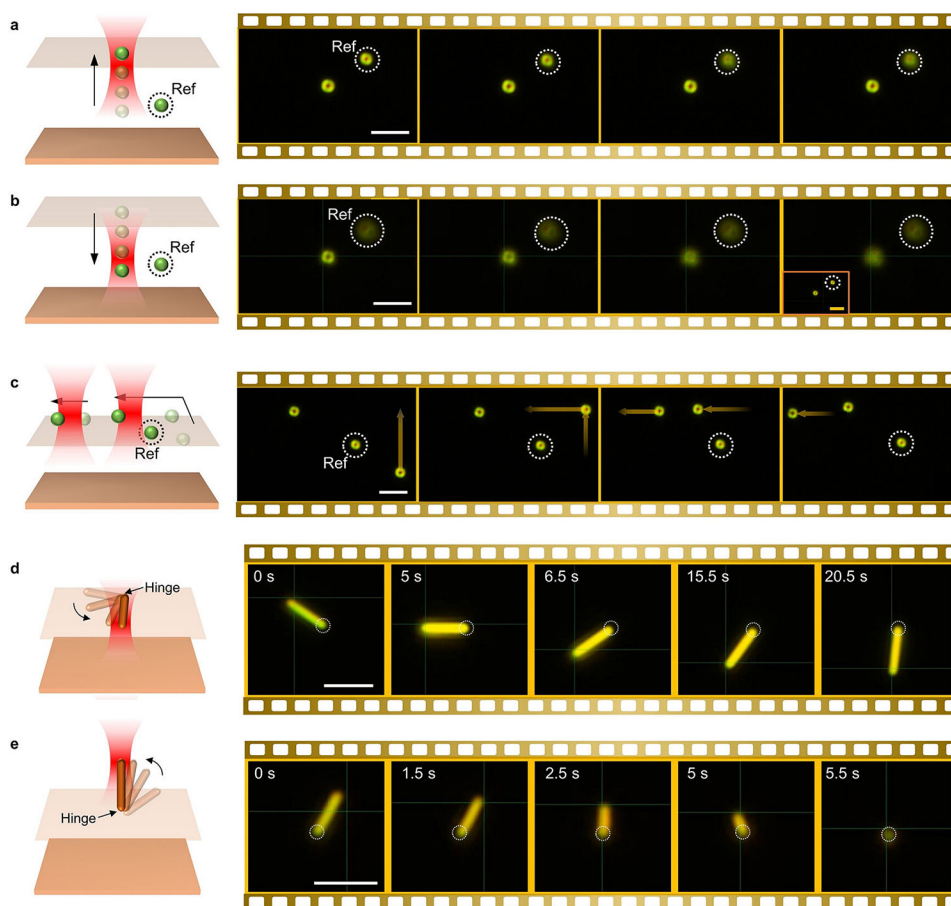
> 250 nm). The black arrows indicate the direction of particle motion, and the red arrow indicates the laser beam propagation direction.
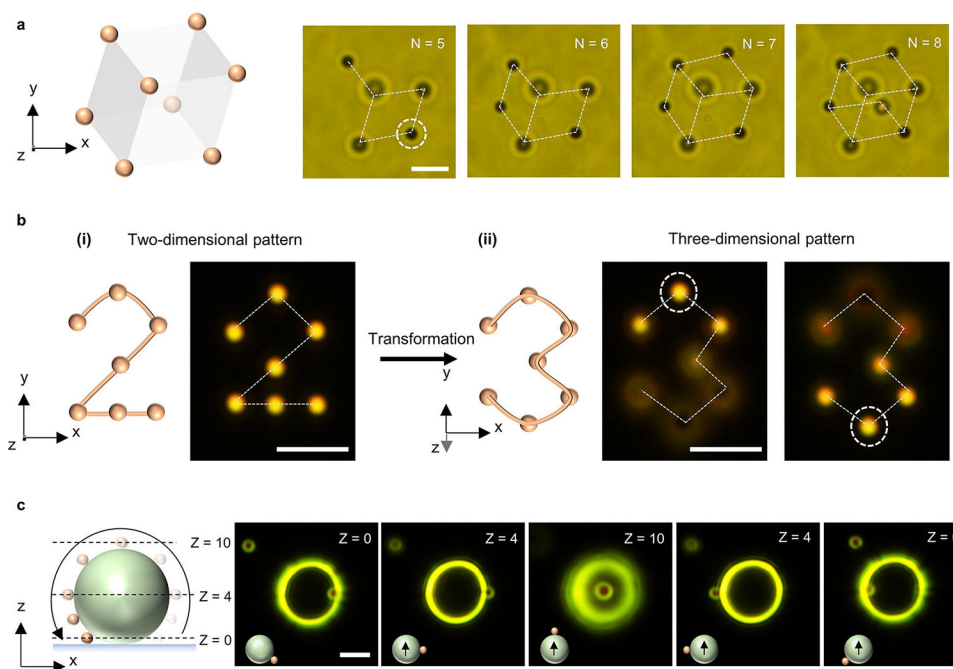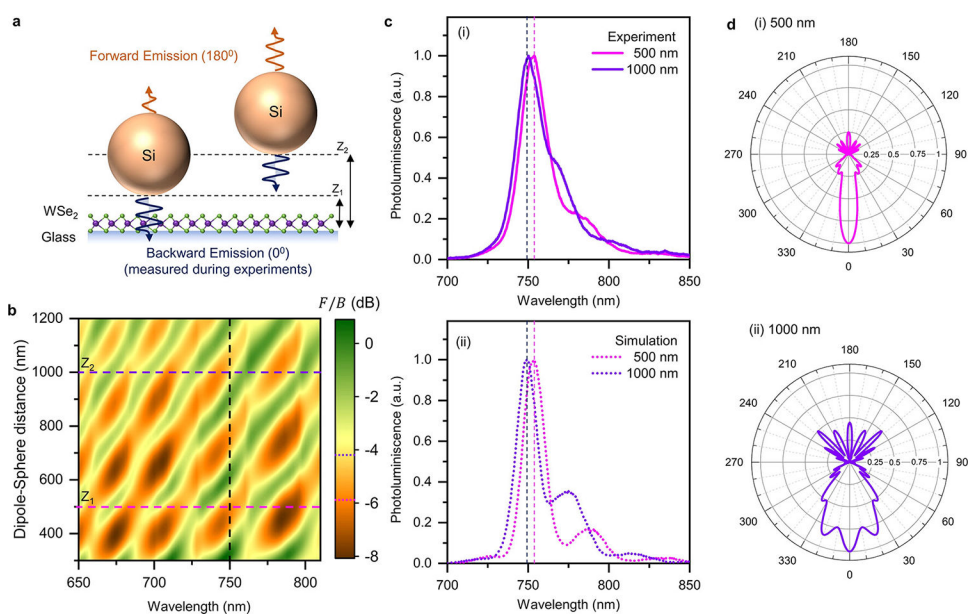
Figure 2.
3D holonomic control of Si microparticles using OMPC: Schematic and dark-field optical microscopy images of (a) pushing along and (b) pulling 1.5 μm Si particles against the laser beam propagation direction (inset in last panel: focal plane at the reference particle); (c) nudging 1.5 μm Si particles in-plane perpendicular to the laser beam propagation direction; (d) in-plane (azimuthal) rotation and (e) out-ofplane (polar) rotation of 5 μm silicon nanowires. Shaded planes in the schematics are the imaging plane for the microscopic images. Particles highlighted in dotted circles are stationary reference particles. Scale bar: 5 μm.

Figure 3.
Versatility of OMPC: (a) Schematic and sequential microscopic images of a 3D array of 1.5 μm Si particles precisely arranged via OMPC. Imaging plane is indicated by the particle highlighted by the dashed circle. All other particles are on different planes but form a cube (dashed lines; also see Supporting Information). (b) Schematic and final optical microscopic images of particles arranged in (i) a twodimensional "2" pattern, which is reconfigured into (ii) a three-dimensional "3" pattern. Particles of the "3" pattern are at varying heights on a tilted virtual plane. The two microscopic images show the same "3" pattern at two different imaging planes where the foci are on the particles highlighted by the dashed circles. (c) Schematic and optical images of a 1.5 μm Si particle manipulated on the surface of a 10 μm PS particle. Position of the imaging plane is highlighted in the upper right corner (unit: μm). The Si particle is manipulated from the left bottom (first panel) to the right bottom (last panel) of the PS particle. The schematics on the bottom right corner show the relative position of the Si particle with respect to the PS particle. Scale bar: 5 μm.

Figure 4.
Tuning light–matter interactions using OMPC: (a) Schematic of a Si particle on a WSe$_2$ monolayer at different heights Z_1 and Z_2 tuned using OMPC. The scattered emission energy in the forward (F, orange) and backward (B, blue) directions change with varying distance. (b) Simulated F/B ratio for varying distances between the particle and WSe$_2$. The vertical black dashed line corresponds to the exciton emission wavelength of the WSe$_2$ monolayer. The horizontal dashed lines correspond to the heights of 500 nm (Z_1) and 1000 nm (Z_2), respectively. The F/B ratios at the intersections are −5.7 and −4.1 dB, respectively (highlighted on the color bar). (c) Experimental (i) and simulated (ii) photoluminescence spectra (normalized) indicate the change in the peak position and altered PL emission at 750 nm. (d) Simulated scattered emission from the particle showing that the backward emission is stronger at Z = 500 nm (i) compared to Z = 1000 nm (ii).